ELSEVIER

International Journal of Mass Spectrometry 210/211 (2001) 283–301

International Journal of Mass Spectrometry

www.elsevier.com/locate/ijms

Guided ion beam studies of the state-specific reactions of Cr^+ and Mn^+ with CS_2 and COS

Chad Rue[a], P.B. Armentrout[a,*], Ilona Kretzschmar[b], Detlef Schröder[b], Helmut Schwarz[b]

[a]*Department of Chemistry, University of Utah, Salt Lake City, Utah, 84112, USA*
[b]*Institut für Organische Chemie der Technischen Universität Berlin, Strasse des 17. Juni 135, D-10623 Berlin, Germany*

Received 15 December 2000; accepted 10 January 2001

Abstract

Reactions of Cr^+ and Mn^+ with CS_2 and COS are studied using guided ion beam mass spectrometry. The electronic-state distributions of the metal-ion beams are systematically varied to probe the contributions of individual reactant states to the observed overall reactivity. The cross section for MnS^+ formation in the reaction of Mn^+ + COS exhibits two endothermic features corresponding to spin-forbidden formation of ground-state $MnS^+(^5\Pi)$ and spin-allowed formation of excited-state $MnS^+(^7\Pi)$. The cross section for MnS^+ formation in the reaction of $Mn^+ + CS_2$, and the cross sections for CrS^+ formation in the reactions of $Cr^+ + CSX$ (X = O, S) also appear to be composites, although the state-specific product cross sections are not resolved in these three systems. Cross sections for forming $CrCS^+$ and $MnCS^+$ in the CS_2 systems and $CrCO^+$ in the Cr^+ + COS reaction also exhibit two endothermic features, which are assigned to the formation of different structural isomers. From the thresholds associated with forming CrS^+, $CrCS^+$, MnS^+, and $MnCS^+$, we determine $D_0(Cr^+–S) = 2.68 \pm 0.17$, $D_0(Cr^+–CS) = 1.69 \pm 0.06$, $D_0(Mn^+–S) = 2.52 \pm 0.24$, and $D_0(Mn^+–CS) = 0.83 \pm 0.22$ eV. Results of the $Cr^+ + CS_2$ reaction suggest that the initial step in the activation of CS_2 by Cr^+ is insertion of the metal ion into one of the C–S bonds. (Int J Mass Spectrom 210/211 (2001) 283–301) © 2001 Elsevier Science B.V.

Keywords: Chromium sulfide; Manganese sulfide; State specific; Sulfur transfer

1. Introduction

Transition-metal sulfides play an important role in both biochemical and industrial processes. Sulfides of vanadium, iron, nickel, copper, zinc, molybdenum, and tungsten promote important chemistry in various proteins and enzymes [1–5]. In industrial applications, transition-metal sulfides are used in a wide range of disciplines, including lubrication, energy storage, and catalysis [1]. Beyond these applications, the gas-phase chemistry of transition-metal sulfides has proven to be complex and fascinating. The reactions of V^+ with COS and CS_2 [6], for example, exhibit unusual kinetic-energy dependences that are attributed to competitive spin-allowed and spin-forbidden pathways in product formation. Such electronic-state effects appear to be common in transition-metal sulfur systems, and may be partially responsible for their chemical utility and versatility.

*Corresponding author. E-mail: armentrout@chemistry.utah.edu

Dedicated to Professor Nico M.M. Nibbering in recognition of his outstanding contributions to gas-phase ion chemistry.

PII S1387-3806(01)00400-6

The present work is part of an ongoing collaborative project to systematically examine the reactions of transition-metal ions with the sulfur-transfer reagents CS_2 and COS. A particular interest in this work is to provide an accurate compilation of metal–sulfide bond energies. Previous work has established the thermochemistry of scandium [7], titanium [7], vanadium [6,8], and iron [9] sulfide cations and shown that reactions of atomic metal ions with CS_2 and COS provide reliable metal sulfide cation bond energies. (For a general discussion of the periodic trends of first and second-row transition-metal sulfides, see [10].) The mechanism of these reactions was investigated most thoroughly in the case of vanadium [6] where a combination of theory and experiment was used to establish that the reactions proceed by insertion into the CS bond. This latter work also demonstrated the effects of different electronic states of the reactants and the production of different electronic states of the metal sulfide cation products. In the present work, we extend these studies to the reactions of chromium and manganese cations. As in our work with vanadium [6], particular care is taken to characterize the reactivity of different electronic states of the metal cations.

2. Experimental methods

2.1. Guided ion beam mass spectrometer

The experiments were performed with a guided ion beam mass spectrometer, which has been described in detail previously [11,12]. Briefly, M^+ (M = Cr, Mn) ions are formed in one of several interchangeable ion sources, as described in the following. Ions produced in the source are accelerated and passed through a magnetic sector for mass selection. The mass-selected ion beam is then focused into the entrance of a radio-frequency (rf) octopole ion guide, whose dc potential with respect to the ion source determines the kinetic energy of the ion beam. The rf potential on the octopole rods radially confines the ions and guides them through a gas cell, where a neutral reactant is introduced at pressures low enough (0.05–0.2 mTorr) to ensure single collision conditions. Both product and unreacted primary ions are extracted from the octopole and passed through a quadrupole for mass analysis. Finally, ions are detected with a secondary-electron scintillation ion detector using standard pulse-counting techniques. Different collision energies are achieved by adjusting the dc octopole potential with respect to the ion source. Conversion of the raw ion intensities into cross sections and the calibration of the absolute energy scale are treated as described previously [11]. The accuracy of the product cross-section magnitudes is estimated to be ± 20%, and the uncertainty in the absolute energy scale is ± 0.05 eV (lab). Laboratory energies are converted to energies in the center-of-mass frame using

$$E = E_{lab}M/(M + m) \quad (1)$$

where M and m are the masses of the neutral and ionic reactants, respectively. This procedure accounts for conserving the momentum of the center-of-mass of the collision pair through the laboratory. Consequently, some energy is not available to the system to induce chemical changes.

Energy thresholds for product formation at 0 K, E_0, are obtained by modeling the cross sections using

$$\sigma(E) = \sigma_0 \Sigma g_i (E + E_i - E_0)^n / E^m \quad (2)$$

where σ_0 is an energy-independent scaling factor, E is the relative kinetic energy, and E_0 and n are treated as adjustable fitting parameters. The summation is over the rovibrational states of the neutral reactant having energies E_i and populations g_i. The parameter m is typically held at unity [13]; however, a value of m = 1.5 may be appropriate for spin-forbidden processes [6]. In the present work, many of the reactions are spin-forbidden, as discussed in fhe following. Each of these spin-forbidden processes is modeled using Eq. (2) with m = 1.5 in addition to m = 1.

2.2. Ion sources

Two ion sources are used to produce M^+ ion beams with different electronic state distributions. First, a dc discharge sputtering source is used in which energetic Ar^+ ions sputter M^+ ions from a

Table 1
Electronic state distributions (%) at various temperatures[a]

Ion	State	Configuration	Energy (eV)[b]	1550 K	1800 K	2050 K	2200 K	2350 K
Cr^+	$a\ ^6S$	$3d^5$	0	99.994	99.972			
	$a\ ^6D$	$3d^4\ 4s$	1.522	0.006	0.028			
	Higher states	···	>2.458	<0.001	<0.001			
Mn^+	$a\ ^7S$	$3d^5\ 4s$	0			99.895	99.829	99.737
	$a\ ^5S$	$3d^5\ 4s$	1.175			0.092	0.145	0.216
	$a\ ^5D$	$3d^6$	1.808			0.013	0.026	0.048
	Higher states	···	≥3.418			<0.001	<0.001	<0.001

[a] Boltzmann distributions at indicated temperatures.
[b] Energies are weighted averages (by degeneracies) over J levels, taken from [26].

negatively charged (from −1.5 to −2 kV) cathode composed of the metal to be studied. The ions formed in this source are then swept through a meter-long flow tube by 10% argon in helium buffer gas at a total pressure of 0.7–1.0 Torr. The ions undergo ~10^5 collisions with the buffer gas as they traverse the flow tube, which helps to cool the ions to room temperature. However, it has been shown that helium and argon are not always effective at quenching the excited electronic states of transition-metal ions [6–9,14–18]. Therefore, small amounts (40 mTorr or less) of a suitable cooling gas may also be added to the flow tube. The ideal cooling gas reacts efficiently at room temperature with all of the excited electronic states of the metal ion but not with the ground state. Thus, a pure ground-state M^+ beam can be obtained at the exit of the flow tube. Both methane and COS are used as cooling gases in this study.

The second ion source used in this study is a surface ionization (SI) source, in which CrO_2Cl_2 or $MnCl_2$ vapors are exposed to a resistively heated rhenium filament. For the Cr^+ experiments, liquid CrO_2Cl_2 precursor is admitted to the vacuum chamber through a leak valve. For the Mn^+ experiments, solid $MnCl_2$ is used as the precursor. Because of its low volatility, the $MnCl_2$ must be heated in an oven near the filament. The metal-containing compound decomposes on the hot filament, and M^+ ions desorb with an electronic-state distribution characteristic of the filament temperature. The filament temperature was previously calibrated as a function of the applied current using optical pyrometry and the assumption that the filament acts as a blackbody radiator [19]. In this work, the filament temperatures range from 1550 to 1800 K in the Cr^+ experiments and from 2050 to 2350 K for Mn^+. At these temperatures, the Cr^+ beam is nearly pure $Cr^+(^6S)$ ground state because of the large energy difference between the ground and first excited states of Cr^+ (Table 1). At 2050 and 2350 K, the total excited-state Mn^+ populations are 0.105% and 0.263%, respectively (Table 1). Lower temperatures could not be used for Mn^+ in this work, because they resulted in unacceptably low ion intensities.

2.3. Theoretical calculations

Calculations to ascertain the ground and excited electronic states of CrS^+ and MnS^+ were performed using the Amsterdam density functional (ADF, version 2.0.1) suite of programs [20–22]. Geometry optimizations were performed with the inner-shell electrons ([Ne] for S, Cr, and Mn) treated in the frozen core approximation [23] with triple-zeta basis sets. All energies are calculated using the local spin density approximation with Slater's exchange functional and the Vosko-Wilk-Nusair parameterization [24] augmented by Becke's and Perdew's (BP) gradient corrections for the exchange and correlation potential, respectively [25]. This method will be referred to as ADF/BP86. Although the accuracy of the absolute energies in ADF is not completely satisfactory, the program does provide control over the symmetry of the wave function, thereby permitting a proper description of excited states.

3. Results and discussion

3.1. M^+ reactant state considerations

Before any quantitative thermodynamic information can be extracted from our experiments, the internal state distributions of both the ionic and neutral reactants must be characterized. The presence of any populated excited states adds extra energy to the reaction system that, unaccounted for, leads to erroneous threshold measurements. In these experiments, the translational, rotational, and vibrational energies of the CS_2 and COS reactants are calculated as Boltzmann distributions at 300 K. The internal electronic energies of the Cr^+ and Mn^+ reactants are also calculated as Boltzmann distributions in SI experiments, because previous studies have shown that these distributions are well characterized by the filament temperature [6,19]. The state distributions of ions produced in the dc discharge/flow tube (dc/FT) source are not as straightforward to determine. As mentioned above, we often observe the presence of excited-state ions produced in our dc/FT source even though the ions undergo thousands of collisions with the helium/argon buffer gas. The final state distribution of these ions is difficult to ascertain, and may not be characterized by a temperature. In this regard, we usually monitor the state distribution by observing the effect of the ion source conditions on the product cross sections. In the work presented here, the MS^+ cross sections obtained in the reactions with CS_2 and COS provide a convenient probe for monitoring the presence of electronically excited M^+ ions in the reactant beam.

3.1.1. Electronic states in Cr^+ beams

The low-energy regions of the cross sections for forming CrS^+ in

$$Cr^+ + CS_2 \rightarrow CrS^+ + CS \quad (3)$$

$$Cr^+ + COS \rightarrow CrS^+ + CO \quad (4)$$

are shown in Figs. 1 and 2, respectively. When the reactions are performed with the SI source, both cross sections exhibit single features that rise from the thresholds and increase with increasing energy, characteristic of endothermic processes. In both cases, there is an extremely small amount of reactivity observed below these thresholds. We believe that these data points correspond to background counting noise in both systems, primarily because residual excited states should have a larger cross section in the COS system than in the CS_2 system, and we observe the opposite result. The threshold to form CrS^+ in the COS reaction is lower than in the CS_2 reaction, simply because the C–S bond energy in COS (3.14 eV, Table 2) is lower than in CS_2 (4.50 eV, Table 2).

When the dc/FT source is used without adding a cooling gas to the flow tube, both reactions behave the same at high energies but also yield additional low-energy features that decrease with increasing energy, behavior characteristic of exothermic processes. These low-energy features must result from reactions of electronically excited Cr^+ ions that survive the collisions in the flow tube. Addition of methane to the flow tube quenches some of these states. In the reaction with COS (Fig. 2), the residual electronic states still exhibit exothermic reactivity. The higher C–S bond energy of CS_2 renders the reaction of these excited states endothermic, such that they appear as a low-energy shoulder on the ground-state cross section. A closer examination of Fig. 1 shows that the energy difference between the thresholds of the two endothermic features in the $CrS^+ + CS$ cross section is close to the known state separation of 1.48 eV between the $Cr^+(^6S)$ ground state and the lowest spin-orbit level ($J = 5/2$) of the $Cr^+(^6D)$ first excited state [26]. Therefore, we attribute the low-energy endothermic feature in Fig. 1 to the reaction of the $Cr^+(^6D)$ first excited state. The exothermic feature shown in Fig. 1 must result from reaction of $Cr^+(^4D)$ and higher states. These states are known to react efficiently with CH_4 at thermal energies [27–31].

In the Cr^+/COS system (Fig. 2), none of the excited states are distinguishable, because all of them react exothermically. This observation indicates that COS could be used as its own cooling gas, and results for such conditions are also shown in Fig. 2. Note that using COS as a cooling gas results in a cross section identical to the SI result, and indicates that a ground

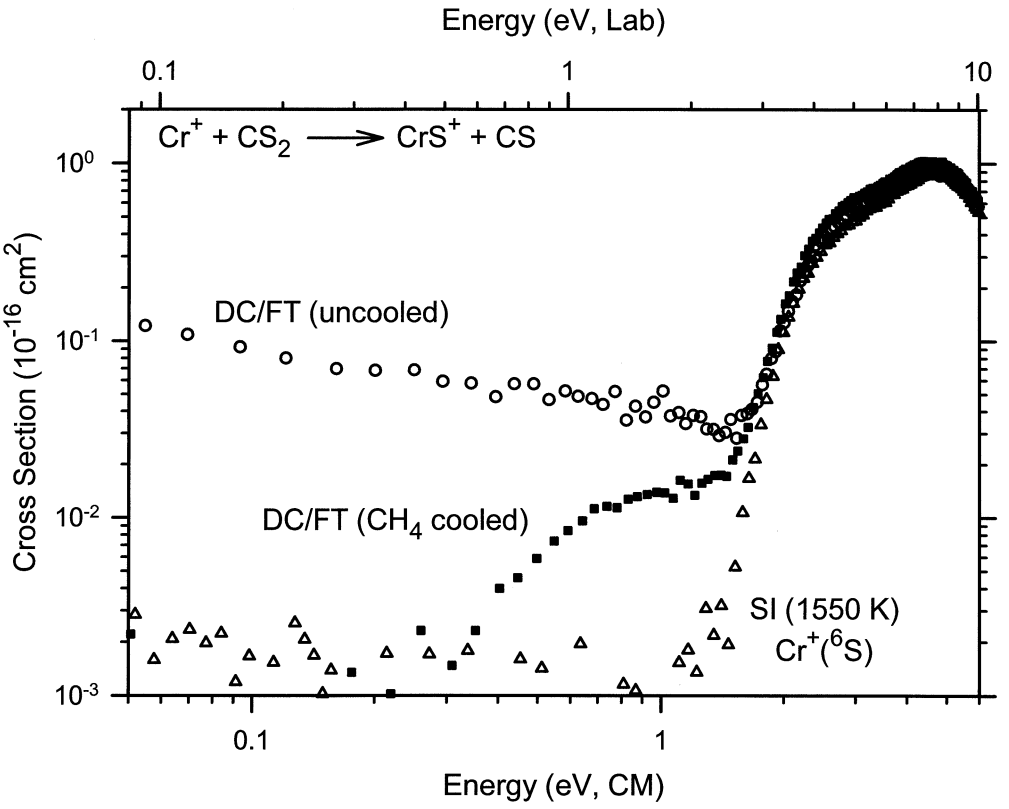

Fig. 1. Cross sections for CrS^+ formation in reaction (3) as a function of kinetic energy in the center-of-mass (lower axis) and the laboratory (upper axis) frames. The results show that the ionization conditions affect the cross section at low energies. The uncooled dc/FT source (open circles) produces the most excited-state ions and the SI source at 1550 K (open triangles) produces the least. The small endothermic feature visible from 0.3 to 1.5 eV CM in the methane-cooled dc/FT cross section (closed squares) results from the reaction of $Cr^+(^6D)$.

state Cr^+ beam has been achieved by adding COS to the flow tube. Fig. 2 clearly demonstrates that COS is superior to methane as a cooling gas for Cr^+. This result is consistent with previous findings from our laboratory demonstrating that the $Cr^+(^6D)$ first excited state is unreactive towards methane [27,30].

In conclusion, discharge sputtering in flowing afterglow ion sources such as our dc/FT source produces an observable quantity of excited state Cr^+ ions that are not efficiently quenched by helium or argon collisions. Although the exact fraction of excited-state Cr^+ ions is unknown and varies with source conditions, we can obtain an estimate of these populations by comparing the exothermic part of the cross sections to the Langevin-Gioumousis-Stevenson (LGS) model [32], which represents the theoretical collision cross section for ion-induced dipole interactions. LGS cross sections are calculated as $\sigma_{LGS}(E) = \pi e(2\alpha/E)^{1/2}$, where E is the kinetic energy, e is the electron charge, and α is the polarizability of the neutral: $\alpha(CS_2) = 9.1$ Å^3 and $\alpha(COS) = 5.7$ Å^3 [33]. We note that the observed magnitudes of the exothermic features of the cross sections for reactions (3) and (4) when no cooling gas was added to the flow tube are approximately 0.1% of the LGS model. For Cr^+ cooled by methane, the COS system cross section is about 0.05% of the LGS prediction. Because not all collisions may be reactive, these percentages must be regarded as lower limits to the excited state Cr^+ concentrations. With methane present as a cooling gas, the results shown in Fig. 1 indicate that the fraction of excited states above the ^6D is reduced by

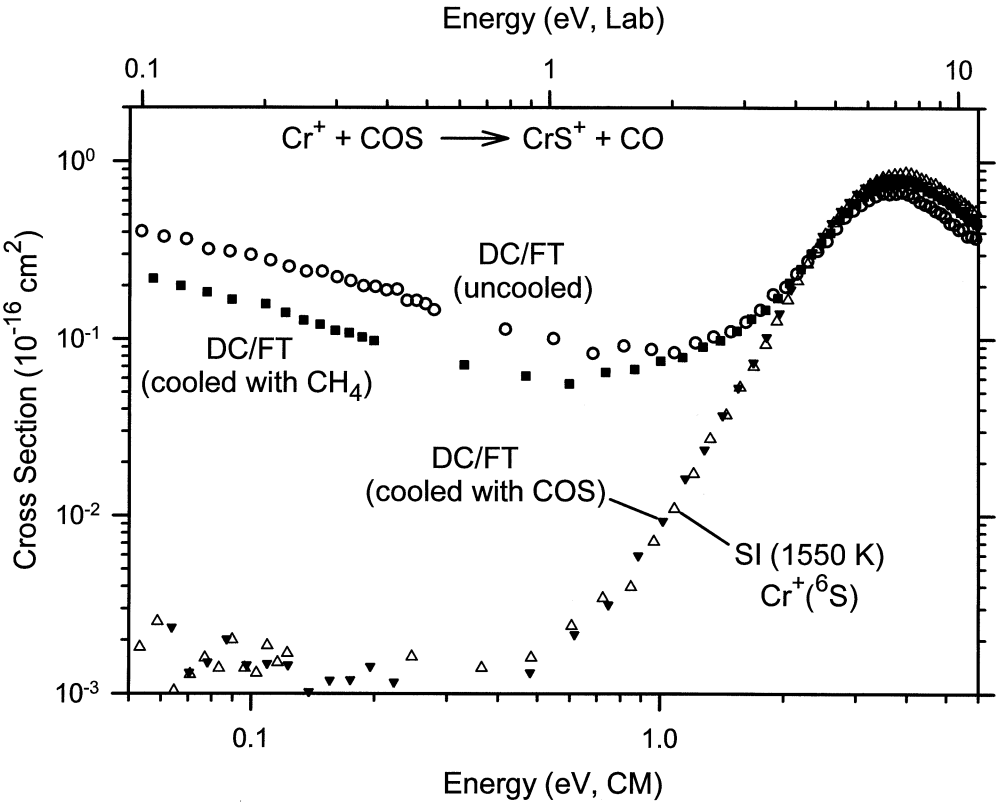

Fig. 2. Cross sections for CrS^+ formation in reaction (4) as a function of kinetic energy in the center-of-mass (lower axis) and the laboratory (upper axis) frames. Adding methane to the flow tube quenches only a fraction of the excited Cr^+ ions produced by the dc/FT source. Cooling with COS, however, yields an identical cross section as the SI source, which produces a nearly pure ground-state $Cr^+(^6S)$ beam.

more than two orders of magnitude, whereas Fig. 2 indicates that only 50% of all excited states are removed by reaction with methane. COS, on the other hand, reduces the contribution of all excited states by more than two orders of magnitude (Fig. 2).

3.1.2. State-specific cross sections of the Cr^+ reactant

The state-specific cross section for forming CrS^+ in the reaction of ground-state $Cr^+(^6S)$ with CS_2 is equivalent to the result obtained with the SI source shown in Fig. 1. As noted above, the low-energy endothermic feature in Fig. 1 obtained with the methane-cooled dc/FT source results from the reaction of residual $Cr^+(^6D)$ excited state ions. An estimate of the absolute magnitude of the $Cr^+(^6D)$ state-specific cross section for CrS^+ formation could be obtained if the population of $Cr^+(^6D)$ ions in the beam were known, which is not the case. However, the magnitude of the $Cr^+(^6S)$ ground-state cross section is largely unaffected by the choice of ion source, which indicates that the $Cr^+(^6D)$ population in the CH_4 cooled dc/FT beam must be low, certainly less than 10%. The results of Fig. 2 indicate that as little as 0.05% of the methane cooled beam could produce the features attributed to $Cr^+(^6D)$. Therefore, the absolute magnitude of the $Cr^+(^6D)$ state-specific cross section must be larger than the feature shown in Fig. 1 by at least a factor of 10 and possibly by as much as a factor of 2000. The energy dependence of this feature, however, is expected to accurately represent the behavior of the $Cr^+(^6D)$ state-specific cross section.

Table 2
Heats of formation and bond dissociation energies at 0 K

Species	$\Delta_f H_0$ (eV)[a]	D_0 (eV)
C	7.371 (0.005)	
O	2.558 (0.001)	
S	2.847 (0.003)	
CO	−1.180 (0.002)	11.109 (0.005)
CS	2.85 (0.04)[b]	7.37 (0.04)
COS (OC–S)	−1.473 (0.003)[c]	3.140 (0.005)
(SC–O)		6.88 (0.04)
CS_2	1.200 (0.008)[c]	4.50 (0.04)
Cr^+	10.863 (0.016)	
Mn^+	10.360 (0.005)	
CrO^+	9.70 (0.12)	3.72 (0.12)[d]
CrS^+	11.03 (0.17)[e]	2.68 (0.17)[e]
MnS^+	10.69 (0.24)[e]	2.52 (0.24)[e]
Cr^+–CO	8.75 (0.04)	0.93 (0.04)[d,f]
Cr^+–CS	12.02 (0.07)[e]	1.69 (0.06)[e]
SCr^+–C	15.5 (0.3)[e]	2.9 (0.3)[e]
Mn^+–CO	8.92 (0.10)	0.26 (0.10)[d]
Mn^+–CS	12.38 (0.22)[e]	0.83 (0.22)[e]

[a] See [50].
[b] See [36].
[c] See [51]. Corrected to 0 K using $H^0 - H^0$ (298.15) values taken from footnote a.
[d] See [43].
[e] This work.
[f] See [49].

3.1.3. Electronic states in Mn^+ beams

The low-energy regions of the cross sections for forming MnS^+ in

$$Mn^+ + CS_2 \rightarrow MnS^+ + CS \quad (5)$$

$$Mn^+ + COS \rightarrow MnS^+ + CO \quad (6)$$

are shown in Figs. 3 and 4, respectively. Interaction of CS_2 with Mn^+ produced in the uncooled dc/FT source yields an exothermic feature (Fig. 3) similar to that observed in the $Cr^+ + CS_2$ reaction (Fig. 1). The magnitude of the exothermic feature in the Mn^+/CS_2 system is 0.6% of σ(LGS), larger than that observed in the Cr^+/CS_2 system. This is presumably because the first excited state of Mn^+ is lower in energy than that of Cr^+ (Table 1). Addition of either methane or COS to the flow tube completely eliminates the exothermic feature in the Mn^+/CS_2 system, which is therefore attributed to the reaction of excited Mn^+. Unlike the results observed for Cr^+, both methane and COS appear to quench the excited states of Mn^+, although we note that relatively large pressures of either gas are required. We needed 20−40 mTorr of methane or COS in this work, compared to 1–5 mTorr of cooling gas typical for other systems. Thus, we assign ions produced in the cooled dc/FT source as ground-state $Mn^+(^7S)$.

Interestingly, the MnS^+ cross section obtained in the reaction of $Mn^+(^7S)$ with COS appears to exhibit two distinct endothermic features below 6 eV. This behavior was reproducible in all of the cooled dc/FT data sets, and therefore, both features must be attributed to the reaction of ground-state $Mn^+(^7S)$. The presence of two endothermic features indicates that MnS^+ is produced in two different processes with different energetics (see the following).

The SI experiments for reactions (5) and (6) reveal the presence of excited states compared to the cooled dc/FT data sets. These excited states react endothermically with CS_2 (Fig. 3) and exothermically with COS (Fig. 4). This different behavior is a result of the different C–S bond strengths in CS_2 and COS (Table 2). The identification of the excited states is discussed in Sec. 3.1.4.

As for Cr^+, we conclude that our dc/FT source produces an observable amount of electronically excited Mn^+ ions that are resistant to collisional quenching with helium or argon. Methane and COS, however, appear to quench these excited states with modest efficiencies.

3.1.4. State-specific cross sections of the Mn^+ reactant

As indicated in Table 1, the SI source produces a nearly pure beam of ground-state $Mn^+(^7S)$ with small amounts of the ^5S and ^5D excited states, and negligible amounts of higher-lying states. The ratios of the SI cross sections shown in Figs. 3 and 4 can be compared with ratios calculated from the populations indicated in Table 1. As is obvious from the raw data, the ratios are near unity at elevated energies. Between 1.2 and 2.4 eV, the cross-section ratios, reported as ratios of the filament temperatures, for reaction (5) are 2350 K/2050 K = 2.1 ± 0.3, 2350 K/2200 K = 1.4 ± 0.2, and 2200 K/2050 K = 1.5 ± 0.3. The ratios for

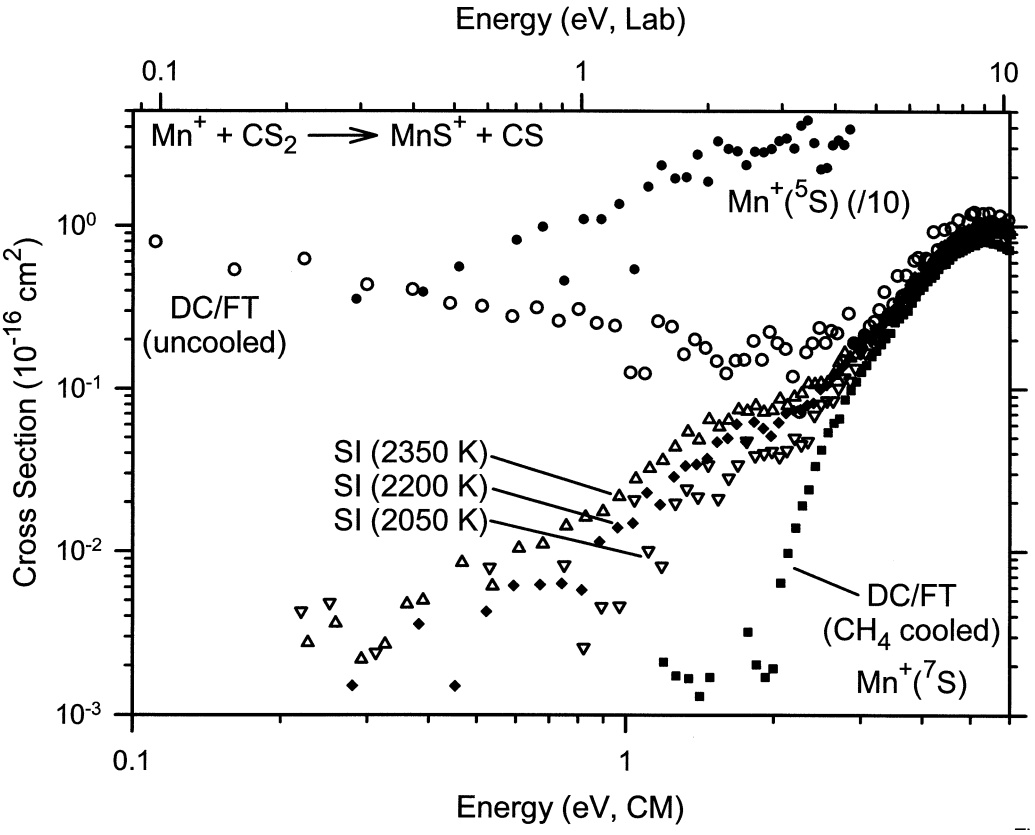

Fig. 3. Cross sections for MnS^+ formation in reaction (5) as a function of kinetic energy in the center-of-mass (lower axis) and the laboratory (upper axis) frames. The addition of COS or methane to the flow tube produces a ground-state $Mn^+(^7S)$ reactant beam (closed squares), while SI produces detectable amounts of excited-state ions. The SI cross sections are extrapolated to estimate the state-specific cross section for the reaction of the $Mn^+(^5S)$ first excited state (closed circles, divided by ten).

reaction (6) between 0.1 and 1.0 eV are 2350 K/2050 K = 2.5 ± 0.3, 2350 K/2200 K = 1.6 ± 0.1, and 2200 K/2050 K = 1.6 ± 0.2. The expected cross section ratios for reaction of the $Mn^+(^5S)$ state in a Boltzmann distribution of electronic states (Table 1) are 2350 K/2050 K = 2.3, 2350 K/2200 K = 1.5, and 2200 K/2050 K = 1.6. The good agreement between these values helps confirm both the filament temperatures and the assumption of a Boltzmann distribution of electronic states.

Although contributions from the ^5D state are almost certainly present, comparison of the ratios indicates that the reactivity observed at low energies can be attributed primarily to the ^5S first excited state. Given this approximation and the ^5S and ^7S populations in Table 1, the SI cross sections can be linearly extrapolated to state-specific cross sections for $Mn^+(^7S)$ and $Mn^+(^5S)$. Such cross sections for the ^7S ground state (not shown) are consistent with those shown for the reaction of Mn^+ formed in the dc/FT (CH_4 cooled) source. Those derived for the $Mn^+(^5S)$ first excited state are shown in Figs. 3 and 4. The cross sections are truncated at higher energies because the extrapolations are noisy in the region where the ground-state reactivity dominates. If a linear extrapolation including the population of the ^5D state is performed, the derived cross sections for the excited states are similar to those shown, but approximately 20% smaller for both systems. Comparison of the maximum magnitudes in the two state-specific cross

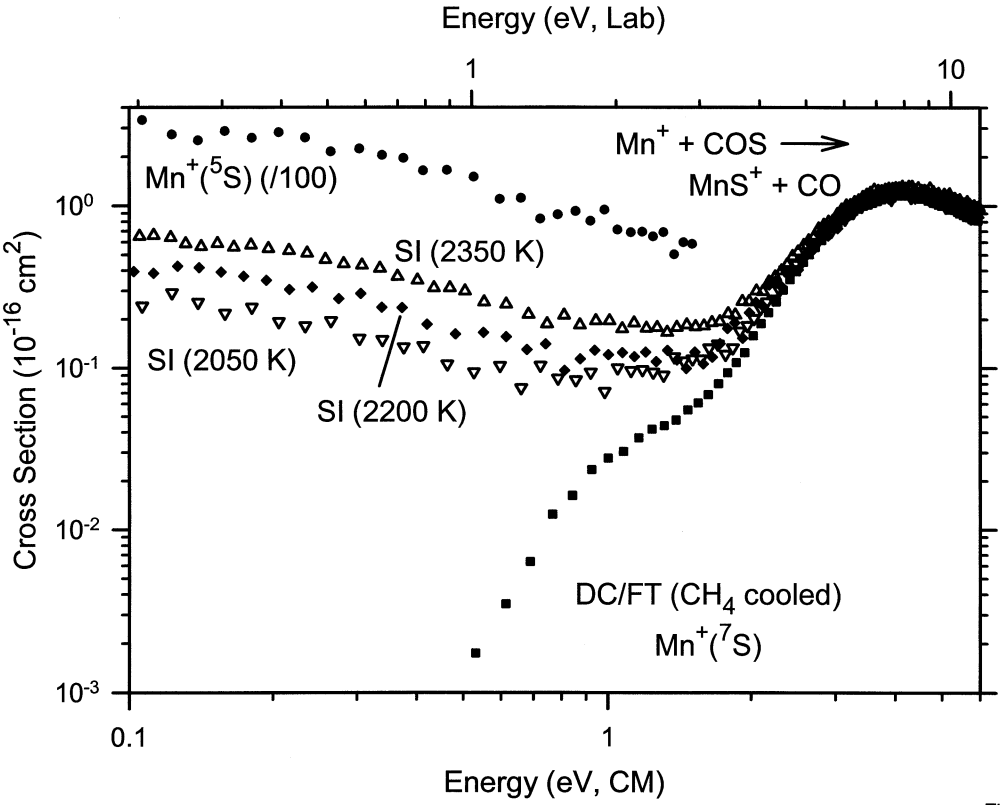

Fig. 4. Cross sections for MnS^+ formation in reaction (6) as a function of kinetic energy in the center-of-mass (lower axis) and the laboratory (upper axis) frames. The reaction of ground-state $Mn^+(^7S)$ produced by the cooled dc/FT source (closed squares) exhibits two endothermic features, attributed to the formation of different electronic states of the MnS^+ product. The SI cross sections are extrapolated to estimate the state-specific cross section for the reaction of the $Mn^+(^5S)$ first excited state (closed circles, divided by 100).

sections for the CS_2 system indicates that the ^5S state is approximately 30 times more reactive than the ^7S ground state.

The energy difference between the thresholds of the extrapolated $Mn^+(^5S)$ and cooled dc/FT cross sections shown for the Mn^+/CS_2 system (Fig. 3) is difficult to determine precisely because of the noise level in the extrapolated $Mn^+(^5S)$ cross section below ~1 eV. Nevertheless, Fig. 3 shows that the energy difference between the thresholds of the endothermic features is in approximate agreement with the known energy separation of 1.2 eV between the ground and first excited states of Mn^+ (Table 1). In Fig. 4, the cross section for $Mn^+(^5S)$ declines with increasing energy, typical behavior for exothermic reactions. This is consistent with the apparent threshold of about 0.5 eV for reaction (6) with $Mn^+(^7S)$ (Fig. 4), which implies that reaction of $Mn^+(^5S)$ should be exothermic by about 0.7 eV. The magnitude of the extrapolated $Mn^+(^5S)$ cross section in reaction (6) is 120% of the locked-dipole collision cross section [34], which is within our experimental uncertainty for absolute cross section magnitudes. This indicates that the reaction occurs on essentially every collision for $Mn^+(^5S)$ ions.

3.2. MS^+ product states

Ab initio calculations (ADF/BP86) indicate that the ground states of CrS^+ and MnS^+ are $^4\Sigma^-$ and $^5\Pi$ states, respectively. Therefore, formation of ground state products from ground state reactants according

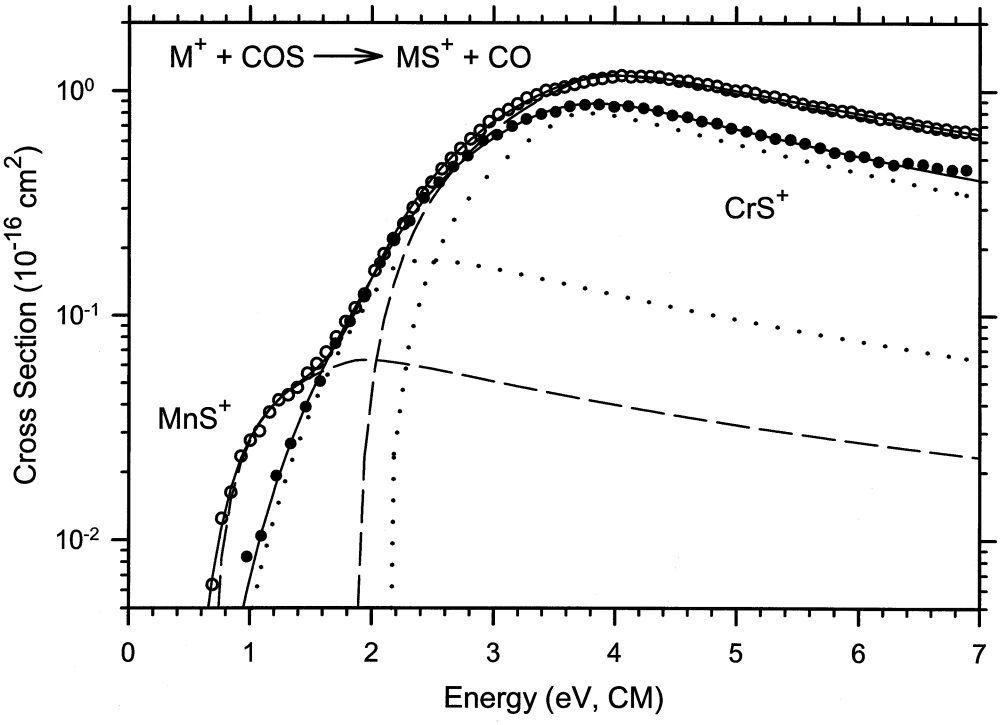

Fig. 5. Cross sections for reactions (4) (closed circles) and (6) (open circles) as a function of kinetic energy in the center-of-mass (lower axis) and the laboratory (upper axis) frames. Dotted (CrS^+) and dashed (MnS^+) lines show speculative models using Eq. (2) for the spin-forbidden reactions (7) and (8) at low energies and the spin-allowed reactions (9) and (10) at high energies. The full lines are the sums of the models convoluted with the kinetic energy distributions of the reactants.

to the following reactions (X = O, S) is spin-forbidden:

$$Cr^+(^6S) + SCX(^1\Sigma^+) \rightarrow CrS^+(^4\Sigma^-) + CX(^1\Sigma^+) \quad (7)$$

$$Mn^+(^7S) + SCX(^1\Sigma^+) \rightarrow MnS^+(^5\Pi) + CX(^1\Sigma^+) \quad (8)$$

Theoretical calculations (ADF/BP86) also indicate that $CrS^+(^6\Pi)$ and $MnS^+(^7\Pi)$ excited states lie 1.52 and 0.47 eV above their ground states, respectively. Formation of these product states according to the following reactions (X = O, S) is spin-allowed:

$$Cr^+(^6S) + SCX(^1\Sigma^+) \rightarrow CrS^+(^6\Pi) + CX(^1\Sigma^+) \quad (9)$$

$$Mn^+(^7S) + SCX(^1\Sigma^+) \rightarrow MnS^+(^7\Pi) + CX(^1\Sigma^+) \quad (10)$$

The primary question with regard to reactions (7) and (8) versus (9) and (10) is the efficiency with which the different electronic states are formed. In each case, formation of the lowest-energy product state is spin-forbidden and might be inefficient if crossing between surfaces of different spin is constrained. At higher energies, spin-allowed pathways become accessible, and an increase in reaction efficiency is reasonable [6].

3.2.1. $Mn^+ + COS \rightarrow MnS^+ + CO$

In the present work, the clearest evidence of multiple MS^+ product states is observed in the Mn^+/COS system. As described above, the MnS^+ cross section exhibits two endothermic features, both of which are assigned to reaction of the $Mn^+(^7S)$ ground state. Fig. 5 illustrates that the efficiency of the two processes is grossly different (about a factor of 20). This behavior is consistent with the spin-forbidden

Table 3
Optmized fitting parameters of Eq. (2)[a]

Reactions	σ_0	E_0 (eV)	n	m
(3) $Cr^+(^6S) + CS_2 \rightarrow CrS^+ + CS$	1.5 ± 0.3	1.80 ± 0.09	1.2 ± 0.2	1
	2.4 ± 0.6	1.77 ± 0.10	1.5 ± 0.3	1.5
(3) $Cr^+(^6D) + CS_2 \rightarrow CrS^+ + CS$	0.020 ± 0.002	0.42 ± 0.11	1.2 ± 0.4	1
	0.024 ± 0.003	0.44 ± 0.11	1.4 ± 0.4	1.5
(4) $Cr^+(^6S) + COS \rightarrow CrS^+ + CO$	0.046 ± 0.016	0.47 ± 0.10	4.0 ± 0.3	1
	0.055 ± 0.014	0.48 ± 0.08	4.4 ± 0.2	1.5
(5) $Mn^+(^7S) + CS_2 \rightarrow MnS^+ + CS$	0.27 ± 0.15	1.91 ± 0.23	2.5 ± 0.4	1
	0.39 ± 0.26	1.83 ± 0.24	2.9 ± 0.5	1.5
(5) $Mn^+(^5S) + CS_2 \rightarrow MnS^+ + CS$	17 ± 4	0.40 ± 0.11	1.8 ± 0.3	1
(6) $Mn^+(^7S) + COS \rightarrow MnS^+ + CO$	0.081 ± 0.014	0.64 ± 0.09	1.4 ± 0.4	1
	0.096 ± 0.03	0.64 ± 0.13	1.7 ± 0.6	1.5
(11) $Cr^+(^6S) + CS_2 \rightarrow Cr^+{-}CS + S$	0.91 ± 0.06	2.81 ± 0.05	1.6 ± 0.1	1
$\rightarrow C{-}Cr^+{-}S + S$	2.2 ± 0.1	6.3 ± 0.2	0.6 ± 0.2	1
(15) $Mn^+(^7S) + CS_2 \rightarrow MnCS^+ + S$	0.35 ± 0.11	3.67 ± 0.22	1.1 ± 0.3	1
(15) $Cr^+(^6S) + COS \rightarrow Cr^+{-}CO + S$	0.14 ± 0.08	1.97 ± 0.24	2.6 ± 0.7	1

[a] Reactions (7) and (8) with X = S are equivalent to processes (3) and (5), respectively, and with X = O, to processes (4) and (6), respectively.

and spin-allowed natures of reactions (8) and (10), respectively.

Along this line of reasoning, the energy difference of the two features corresponds to the adiabatic excitation energy from the $MnS^+(^5\Pi)$ to the $MnS^+(^7\Pi)$ state. Using Eq. (2) to analyze the low energy feature corresponding to reaction (8) (X = O) yields the optimized parameters listed in Table 3, including a threshold of 0.64 ± 0.13 eV (average of $m = 1$ and $m = 1.5$ fits). The threshold of the second feature corresponding to reaction (10) (X = O) is more difficult to analyze because the energy range over which reaction (8) can be modeled before the onset of reaction (10) is small, and the higher-energy behavior of reaction (8) is unknown. This causes a wide range of potentially valid thresholds for reaction (10) (X = O), but most attempts resulted in threshold values ranging from 1.70 to 1.95 eV. A conservative estimate of the high-energy threshold is 1.85 ± 0.20 eV, and an example fit is shown in Fig. 5. In this composite fit, the model for reaction (8) (X = O) has similar parameters to those in Table 3 except that the cross section is assumed to be depleted beginning at the threshold for reaction (10) using a model outlined previously [35]. This model is also used to describe the dissociation of the MnS^+ product, as discussed more thoroughly below. The threshold energy difference of 1.21 ± 0.24 eV determined in this way is considerably larger than the $MnS^+(^7\Pi) \leftarrow MnS^+(^5\Pi)$ adiabatic excitation energy of 0.47 eV obtained by ab initio ADF/BP86 calculations. Thus, either the fitting procedure or the theoretical determination of the state splitting is somewhat in error, or excited states above $MnS^+(^7\Pi)$ are responsible for the observed high-energy feature. We note that it is possible to roughly reproduce the data using Eq. (2) for reactions (8) and (10) (X = O) with the constraint $\Delta E_0 = 0.47$ eV (as suggested by the theoretical results), however, the data are not reproduced with the same fidelity compared to fits having larger ΔE_0 values.

3.2.2. $M^+ + CS_2 \rightarrow MS^+ + CS$, $Cr^+ + COS \rightarrow CrS^+ + CO$

Unlike the MnS^+ cross section observed in the Mn^+/COS system, the MS^+ cross sections observed in the other three systems do not show obvious evidence of two features corresponding to the formation of specific electronic states of the MS^+ products, Figs. 1–3. Nevertheless, the bimodal behavior of the Mn^+/COS system is unambiguous. Further, analogous bimodal behavior was observed for reactions of CS_2 and COS with $V^+(^5D)$ [6], the element immediately preceding Cr^+ in the Periodic Table. Therefore, it seems likely that both MS^+ product states are also

formed in reactions (7)–(10) for the Mn^+/CS_2, Cr^+/COS, and Cr^+/CS_2 systems. In all three systems, the MS^+ cross sections are believed to be composite cross sections with two unresolved features: a lower-energy portion corresponding to the spin-forbidden reactions (7) and (8) and a higher-energy portion corresponding to the spin-allowed reactions (9) and (10). Because the cross sections of the two processes are not resolved, it is impossible to obtain definitive information regarding the higher-energy process. The analyses of the low-energy portions of the data using Eq. (2) are given in Table 3. In all three systems, the interpretation of the low-energy onset is not changed within experimental error whether or not a second high-energy feature is included in the modeling. Including two processes in the modeling results in much better reproduction of the data even though we constrained the thresholds of the second feature as follows. For the Mn^+/CS_2 system, the two models have a threshold difference of 1.21 eV, as suggested by the results of the Mn^+/COS system. For the two Cr^+ systems, the threshold difference of the two models for processes 7 and 9 was held at 1.52 eV during optimization, as suggested by our theoretical results. This restriction is necessary, because the unresolved nature of the features prohibits a direct measurement of the higher-energy threshold. An example of this composite fitting process is shown in Fig. 5 for the Cr^+/COS system. In all three systems, we note that the optimized values of the parameter *n*, which determines the steepness of the fitting curve, was much higher for the low-energy portion than for the high-energy portion. This suggests that the lower-energy process rises more slowly and is less efficient that the higher-energy process, consistent with our assumptions about the spin characteristics of these reactions [3].

3.3. Other product channels

3.3.1. $Cr^+ + CS_2$

In addition to the CrS^+ product, reaction of Cr^+ with CS_2 also yields $[Cr,C,S]^+$ according to

$$Cr^+ + CS_2 \rightarrow [Cr,C,S]^+ + S \quad (11)$$

The square brackets around the $[Cr,C,S]^+$ species indicate that the structural arrangement of the Cr, C, and S atoms is not specified, although it is almost certain that the first feature in the $[Cr,C,S]^+$ cross section corresponds to the Cr^+–CS species in which the metal is bound to an intact thiocarbonyl ligand at the carbon end (see the following). The cross section for $[Cr,C,S]^+$ formation is shown with the accompanying cross section for CrS^+ formation over an extended energy range in Fig. 6. Note that the reactant ions are formed by SI at 1550 K and hence are pure ^6S ground state.

The reaction of $Cr^+(^6S)$ with CS_2 is well behaved, and all of the features in both cross sections are readily explained. The CrS^+ cross section rises from a threshold near 1.5 eV and continues for about 1 eV. At this point, the cross section declines slightly because of the competitive onset of the $[Cr,C,S]^+$ channel. However, the onset for reaction (9) (X = S) is also believed to occur in this energy region [1.52 eV above the threshold for reaction (7), X = S], such that the CrS^+ cross section rises again. Thresholds for the CrS^+ and $[Cr,C,S]^+$ products are analyzed using Eq. (2), yielding values of 1.79 ± 0.12 eV for CrS^+ formation in reaction (3) (average of $m = 1$ and 1.5 fits) and 2.81 ± 0.05 eV for $[Cr,C,S]^+$ formation in reaction (11). Analysis of the reactivity of $Cr^+(^6D)$, Fig. 1, yields a threshold of 0.43 ± 0.11 eV for CrS^+ formation in reaction (3) (average of $m = 1$ and 1.5 fits, Table 3). This threshold is 1.36 ± 0.16 eV below that for reaction of $Cr^+(^6S)$, i.e. consistent with the first excitation energy of Cr^+ within experimental error (Table 1).

The correlation between the CrS^+ and $[Cr,C,S]^+$ channels indicates that they compete directly with each other, evidence that they arise from a common intermediate. Both cross sections begin to decline near 4.5 eV, when dissociation of either product ion becomes energetically possible according to the following overall reaction:

$$Cr^+ + CS_2 \rightarrow Cr^+ + S + CS \quad (12)$$

The $[Cr,C,S]^+$ channel exhibits a second endothermic feature at higher energies. The threshold for this

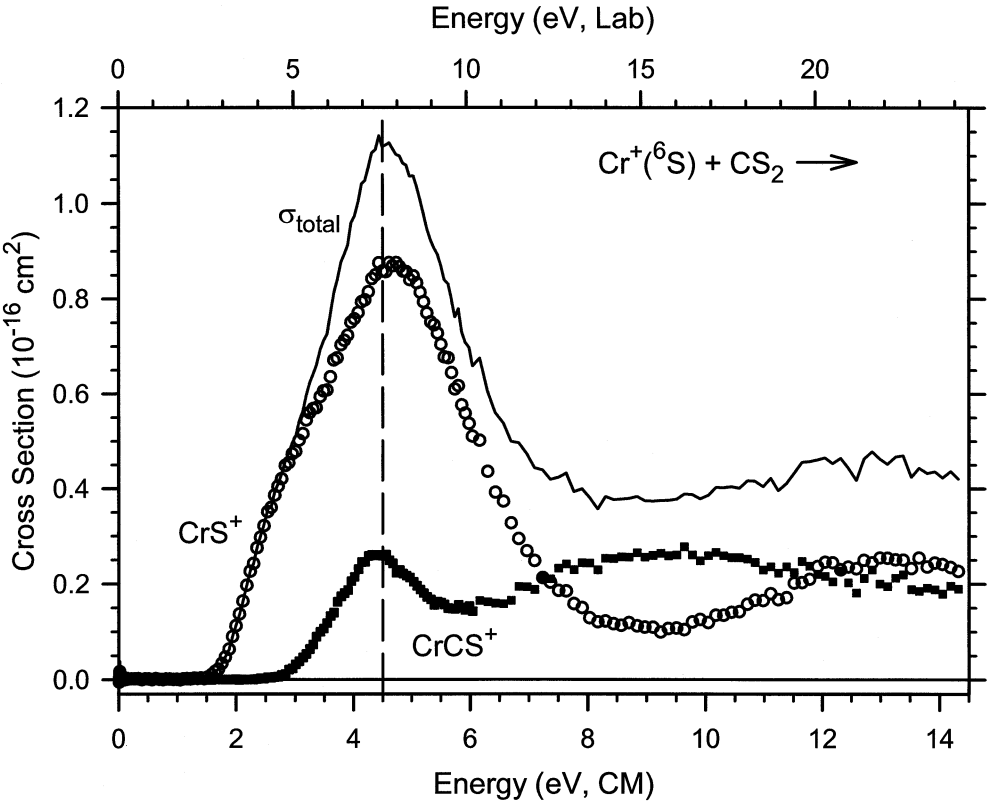

Fig. 6. Cross sections for formation of CrS^+ in reaction (3) (open circles) and $CrCS^+$ in reaction (11) (closed squares) as a function of kinetic energy in the center-of-mass (lower axis) and the laboratory (upper axis) frames. The bond energy of the CS_2 molecule (4.50 eV) is marked by the broken line. Reactant $Cr^+(^6S)$ ions are formed by SI at 1550 K.

process is estimated by subtracting the fit to the first feature (including the dissociation channel 12) [35] and modeling the remainder of the cross section. This yields a threshold estimate of 6.3 ± 0.2 eV (Table 3), which we tentatively assign to the formation of the S–Cr^+–C isomer, in which both C and S atoms are bound directly to the metal. This assignment is supported by the observation that the second feature in the $[Cr,C,S]^+$ channel begins to decline near the onset of a second endothermic feature in the CrS^+ cross section. This correspondence suggests that CrS^+ is formed by simple cleavage of the SCr^+–C bond. Additionally, the energy at which the second feature of the $[Cr,C,S]^+$ cross section declines and the second feature of the CrS^+ cross section rises is consistent with the thermodynamic threshold of 9.19±0.18 eV for

$$Cr^+ + CS_2 \rightarrow CrS^+ + C + S \quad (13)$$

This is 7.37 ± 0.04 eV = D_0(C–S) [36] (Table 2) above the onset of reaction (3).

Although the behavior of the second endothermic feature of the $[Cr,C,S]^+$ cross section seems consistent with assignment to a S–Cr^+–C isomer, we cannot exclude the possibility that formation of an excited electronic state of the Cr^+–CS species or possibly a Cr^+-SC species might explain the second feature.

Finally, the CrS^+ cross section begins to decline again around 13 eV, in reasonable agreement with the

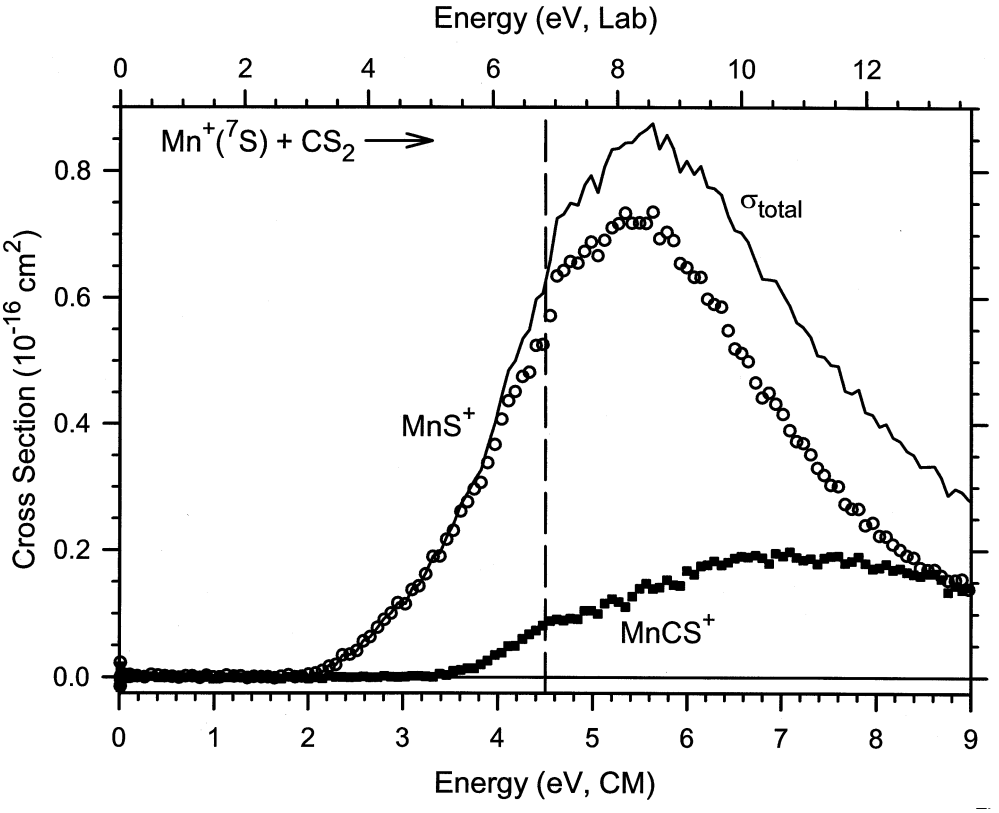

Fig. 7. Cross sections for MnS^+ formation in reaction (5) (open circles) and $MnCS^+$ formation in reaction (15) (closed squares) as a function of kinetic energy in the center-of-mass (lower axis) and the laboratory (upper axis) frames. The bond energy of the CS_2 molecule (4.50 eV) is marked by the broken line.

energetic requirement for complete atomization of the CS_2 molecule at 11.87 ± 0.01 eV according to

$$Cr^+ + CS_2 \rightarrow Cr^+ + C + 2S \quad (14)$$

On the basis of the observed behavior described previously for the Cr^+/CS_2 system, we propose that at least some of the reactive collisions in the Cr^+/CS_2 system proceed via insertion of the metal into one of the C–S bonds of CS_2. Such a mechanism has been previously suggested for the analogous V^+/CS_2 system and is consistent with ab initio calculations of the V^+/CS_2 potential-energy surface [6]. Additionally, Zhou and Andrews [37] have recently observed the formation of neutral metal-inserted S-M-C-S species (M = Co, Ni, and Cu) upon UV photolysis of rare gas matrices containing M atoms and CS_2.

Insertion of Cr^+ into a C–S bond accounts for all of the observed products by sequential bond cleavage of a S–Cr^+–C–S intermediate. Thus, cleavage of the Cr^+–C and S–Cr^+ bonds lead to the low-energy formations of the CrS^+ and Cr^+–CS products, respectively, reactions (3) and (11). At higher energies, rupture of the C–S bond leads to the inserted S–Cr^+–C species, which can decompose further to form CrS^+ in reaction (13).

3.3.2. $Mn^+ + CS_2$

In addition to the MnS^+ species formed in reaction (5), the $[Mn,C,S]^+$ species is also formed in

$$Mn^+ + CS_2 \rightarrow [Mn,C,S]^+ + S \quad (15)$$

The cross section is shown along with the MnS^+ cross section in Fig. 7. Although it is not as evident as for $[Cr,C,S]^+$ (Fig. 6), the $[Mn,C,S]^+$ cross

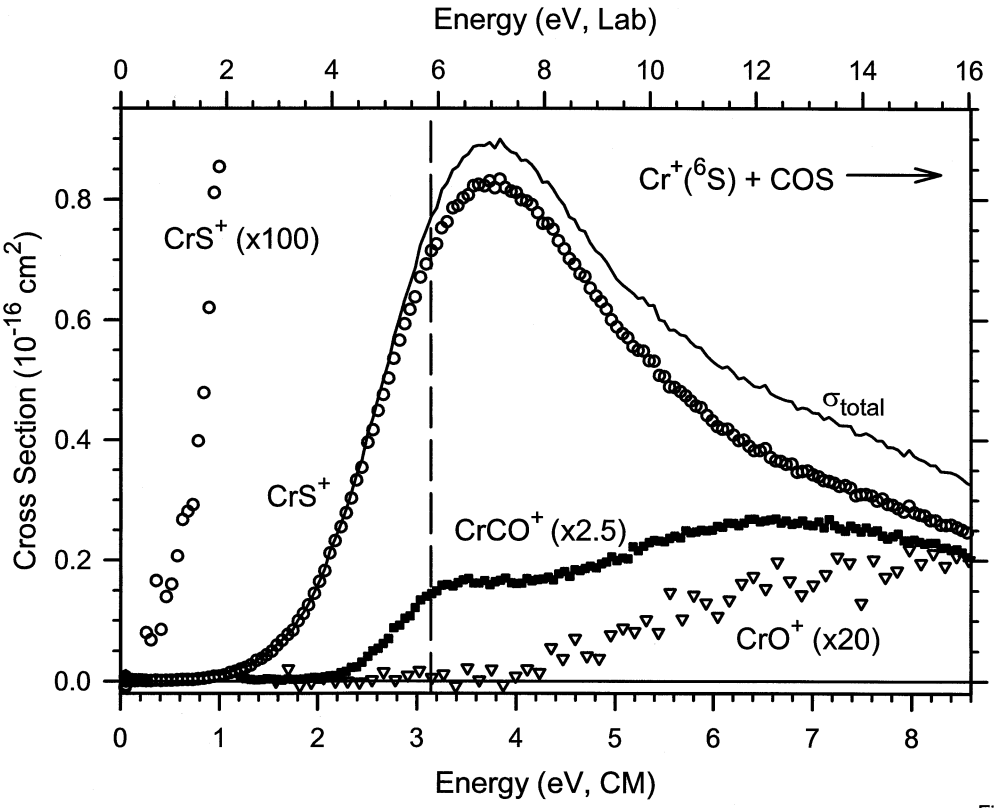

Fig. 8. Cross sections for formation of CrS^+ in reaction (4) (open circles), $CrCO^+$ in reaction 16 (closed squares, multiplied by a factor of 2.5), and CrO^+ (open triangles, multiplied by a factor of 20) as a function of kinetic energy in the center-of-mass (lower axis) and the laboratory (upper axis) frames. The bond energy of the COS molecule (3.14 eV) is marked by the broken line. Reactant $Cr^+(^6S)$ ions are formed by SI at 1550 K. The inset shows the CrS^+ cross section magnified by a factor of 100.

section also appears to be composed of two endothermic features. This cross section levels out at about 4.5 eV, as expected for the onset of the analogue of reaction (12), but then rises again slowly at somewhat higher energies. Analysis of the lowest energy feature of the $[Mn,C,S]^+$ cross section using Eq. (2) yields a threshold of 3.67 ± 0.22 eV (Table 3). The second feature has a threshold near 5 eV, but it is difficult to extract quantitative information about this threshold because of extensive overlap with the first feature. Qualitatively, the small separation between the features in the $[Mn,C,S]^+$ cross section indicates that the Mn^+–CS and putative C–Mn^+–S isomers lie much closer in energy to one another than the analogous Cr^+–CS and C–Cr^+–S isomers (assuming the higher energy feature really can be attributed to the formation of the inserted C–M^+–S species). In particular, judging by their relative thresholds, Cr^+–CS is more stable than Mn^+–CS (as discussed in Sec. 3.4), but C–Mn^+–S is more stable than C–Cr^+–S.

3.3.3 Cr^+ + COS

Three products are observed in the Cr^+/COS system, CrS^+, $CrCO^+$, and CrO^+, as shown in Fig. 8. The cross section for forming $[Cr,C,O]^+$ according to

$$Cr^+ + COS \rightarrow [Cr,C,O]^+ + S \quad (16)$$

shows two endothermic features analogous to those observed in the $[Cr,C,S]^+$ cross section of the Cr^+/

CS_2 system. We again attribute the low and high-energy features to the formation of the Cr^+–CO and C–Cr^+–O isomers, respectively, although there is again the possibility that the second feature may be attributable to an excited electronic state of Cr^+–CO. Note that according to our proposed mechanism (see above), the Cr^+–CO isomer would arise from activation of the S end of the COS molecule (with subsequent S atom loss), whereas the C–Cr^+–O isomer arises from activation of the O end of the COS molecule (with subsequent S atom loss). This distinction is removed in the Cr^+/CS_2 system, because identical S–Cr^+–C–S intermediate species arise from activation of either end of the CS_2 neutral. This is almost certainly a contributing factor to the observation that the magnitude of the $[Cr,C,S]^+$ cross section is larger than that of the $[Cr,C,O]^+$ cross section. Analysis of the low energy feature of the $[Cr,C,O]^+$ cross section with Eq. (2) yields a threshold of 1.97 ± 0.24 eV (Table 3).

Formation of a C–Cr^+–O isomer suggests that fragmentation at higher energies should lead to $CrO^+ + C + S$ and $CrC^+ + O + S$ product pathways. However, the thermodynamic thresholds for these processes are higher than the maximum experimental energies examined. Formation of the $CrO^+ + C + S$ channel, for example, requires 10.53 ± 0.12 eV (Table 2). Formation of $CrO^+ +$ CS is observed at lower energies, although the cross section is noisy and very small (<0.02 Å^2). The threshold for forming this product is difficult to determine, but lies in the vicinity of 4 ± 0.5 eV. This is somewhat higher than the thermodynamic threshold of 3.16 ± 0.13 eV for this process (Table 2). The delayed threshold may be the result of severe competition with the other dominant channels or could indicate a barrier in excess of the reaction endothermicity.

Unlike Fig. 6 for the Cr^+/CS_2 system, the CrS^+ cross section observed in the Cr^+/COS system (Fig. 8) does not show an additional feature at higher energies. This is a consequence of the very strong C–O bond energy in COS (Table 2), which pushes the threshold for $CrS^+ + C + O$ formation to 11.57 ± 0.17 eV, beyond the energy range studied here.

3.3.4. $Mn^+ + COS$

We could not detect formation of $MnCO^+$ in the Mn^+/COS system. If this species forms, it does so very inefficiently. This may be explained by examining the relative bond strengths of the MnS^+ and $MnCO^+$ species, 2.52 ± 0.24 and 0.26 ± 0.12 eV, respectively (Table 2). If COS activation involves an S–Mn^+–C–O intermediate, as described previously for the Cr^+/COS system, it seems reasonable that formation of $MnS^+ + CO$ would dominate over $MnCO^+ + S$, simply because the Mn^+–S bond is much stronger than the Mn^+–CO bond. In the other systems examined in this work, the M^+–S bonds are also stronger than the M^+–CX bonds, but the differences are not as pronounced, i.e. $D_0(Cr^+–CS)/D_0(Cr^+–S) = 0.63$, $D_0(Cr^+–CO)/D_0(Cr^+–S) = 0.35$, and $D_0(Mn^+–CS)/D_0(Mn^+–S) = 0.33$ compared to $D_0(Mn^+–CO)/D_0(Mn^+–S) = 0.10$.

3.4. Thermochemistry

Our previous studies of the V^+/CS_2 system [6] suggested that spin-forbidden reactions are analyzed best using a form of Eq. (2) with $m = 1.5$. Table 3 demonstrates that the threshold energies for the present systems are insensitive to the choice of m (largely because n changes to compensate). This result indicates that Eq. (2) is capable of providing accurate thermochemistry even when the spin characteristics of a reaction are unknown, at least for slowly rising cross sections such as those observed here for CrS^+ and MnS^+ formation. In cases where the cross section rises rapidly from threshold, such as that for formation of VS^+ in the reaction of $V^+(^5D)$ with CS_2, accurate reproduction of the cross section over an extended energy range necessitates the use of $m = 1.5$ [6].

Accordingly, we average the thresholds obtained with $m = 1$ and 1.5 in the evaluation of the thermodynamics of species formed in spin-forbidden processes. From the threshold of reaction (3), $E_0(3) = 1.79 \pm 0.13$ eV, the bond energy of CrS^+ can be calculated as $D_0(Cr^+–S) = D_0(SC–S) - E_0(3) = 2.71 \pm 0.13$ eV. Similarly, $D_0(Cr^+–S)$ can be independently calculated from the threshold of reaction

(4), $E_0(4) = 0.48 \pm 0.11$ eV, yielding $D_0(Cr^+–S) = 2.66 \pm 0.11$ eV. The weighted average [38] of these two results is $D_0(Cr^+–S) = 2.68 \pm 0.17$ eV. From the thresholds associated with reactions (5) and (6), $E_0(5) = 1.87 \pm 0.28$ and $E_0(6) = 0.64 \pm 0.13$ eV, we calculate $D_0(Mn^+–S) = 2.63 \pm 0.28$ and 2.50 ± 0.13 eV, which give a weighted average of 2.52 ± 0.24 eV. The uncertainties in the weighted averages are reported as a conservative error of two standard deviations of the mean for both $D_0(Cr^+–S)$ and $D_0(Mn^+–S)$. It should be noted that the direct correspondence between the thresholds and the bond energies assumes that there are no barriers in excess of the endothermicities of these reactions. In previous work [7–9], measurement of $M^+–S$ bond energies from reactions analogous to processes (3)–(6) has proven to yield accurate thermochemistry on the basis of comparisons to values extracted in alternate experiments. It seems likely that this is also the case for M=Cr and Mn.

From the low-energy thresholds associated with the formation of $CrCS^+$ and $MnCS^+$ in the CS_2 systems (Table 3), we calculate $D_0(Cr^+–CS) = 1.69 \pm 0.06$ and $D_0(Mn^+–CS) = 0.83 \pm 0.22$ eV, respectively. Again, these values are derived assuming that there are no barriers in excess of the endothermicities of these reactions. Further, there is the possibility of competition between the $MCS^+ + S$ reaction channel and the favored $MS^+ + CS$ reaction channel. This could increase the apparent threshold for the former reaction [9], leading to $M^+–CS$ bond energies that are most conservatively viewed as lower limits. However, the former value seems reasonable in light of recent work from our laboratories that determined $D_0(V^+–CS) = 1.70 \pm 0.08$ eV [6,8]. The large difference between the $M^+–CS$ bond energies for Cr^+ and Mn^+ is similar to the previously measured isoelectronic $M^+–CO$ bonding energies for these metals: $D_0(Cr^+–CO) = 0.93 \pm 0.04$ eV and $D_0(Mn^+–CO) = 0.26 \pm 0.10$ eV (Table 2). In both cases, the difference can be explained by the different electron configurations of the metal ions. $Cr^+(^6S)$ has a $3d^5$ valence-electron configuration, whereas $Mn^+(^7S)$ has a $4s^13d^5$ configuration. Consequently, Cr^+ has an empty 4*s* orbital into which the electron pair of the CX ligand (X = S, O) can be donated, whereas Mn^+ has no empty valence orbitals. The CS bond energies exceed those for CO because the CS ligand is more polarizable than CO [39], and because CS is a better σ donor and π acceptor than CO, as revealed by an analysis of the molecular orbitals [40–42].

We might also have assigned the low-energy feature in the $[Cr,C,S]^+$ cross section to an inserted $C–Cr^+–S$ structure, in which case the threshold of 2.81 ± 0.05 eV equals $D_0(SC–S) + D_0(C–S) – D_0(Cr^+–S) – D_0(SCr^+–C)$. This gives $D_0(SCr^+–C) = 6.38 \pm 0.19$ eV, which is unreasonably large compared to previous work that has established the bonding of Cr^+ to other ligands. For example, $D_0(Cr^+–O) = 3.72 \pm 0.12$ eV, $D_0(Cr^+–CH) = 3.04 \pm 0.30$ eV, $D_0(Cr^+–CH_2) = 2.24 \pm 0.04$ eV, and $D_0(Cr^+–CH_3) = 1.14 \pm 0.03$ eV [43]. Further, a $D_0(SCr^+–C)$ of 6.38 ± 0.19 eV would be much higher than any other transition-metal carbide bond determined so far: $ScC^+ = 3.34 \pm 0.06$ eV, $TiC^+ = 4.05 \pm 0.24$ eV, $VC^+ = 3.83 \pm 0.05$ eV [44,45], $FeC^+ = 4.68 \pm 0.30$ eV, and $CoC^+ = 3.59 \pm 0.30$ eV [46]. We therefore assign the low-energy feature in the $[Cr,C,S]^+$ cross section to the $Cr^+–CS$ isomer.

However, from the threshold for the second feature in the $[Cr,C,S]^+$ cross section (Table 3), we calculate $D_0(SCr^+–C) = 2.9 \pm 0.3$ eV, which assumes that the second feature results from the formation of the metal-inserted $C–Cr^+–S$ species. Although this value is somewhat speculative, because we have only circumstantial evidence supporting this assignment, it is reasonable compared to the other transition-metal carbide and chromium-ligand bond energies noted above. If this assignment is correct, it is interesting to note that $D_0(SCr^+–C)$ is approximately equal to $D_0(Cr^+–S)$. This is in agreement with previous studies that determined $D_0(Cr^+–O) = 3.72 \pm 0.12$ eV [47] and $\Delta_f H°(CrO_2^+) = 9.06 \pm 0.52$ eV [48], which leads to $D_0(OCr^+–O) = 3.2 \pm 0.5$ eV. Because the strength of the second $Cr^+–O$ bond is not highly affected by the first O ligand, we may anticipate a similar effect for the $SCr^+–C$ and $Cr^+–S$ bonds. This seems reasonable, given that chromium can support high oxidation states. Finally, from the threshold for

$CrCO^+$ formation in the Cr^+ + COS reaction, we calculate $D_0(Cr^+–CO) = 1.17 \pm 0.25$ eV, which is less precise but well within experimental uncertainty of $D_0(Cr^+–CO) = 0.93 \pm 0.04$ eV [43,49].

4. Summary

In this work, results of the reactions of Cr^+ and Mn^+ generated in several ion sources with CS_2 and COS are reported. Because of the large separation between the ground and first excited state of chromium, the SI source produces a nearly pure ground-state $Cr^+(^6S)$ beam. The cross section for CrS^+ formation obtained using the dc/FT source with methane cooling gas exhibits a small low-energy feature as a shoulder of the ground-state $Cr^+(^6S)$ cross section, which we attribute to reaction of residual $Cr^+(^6D)$ ions that are not quenched in the flow tube. The states of Mn^+ are more closely spaced than those of Cr^+, and the SI source produces a mixture of states with cross sections that can be extrapolated to obtain state-specific information. All these excited states can be quenched in the dc/FT source using either methane or COS as a cooling gas. Using this technique, we estimate the shape of the cross sections for forming MnS^+ in the reaction of ground-state $Mn^+(^7S)$ and excited-state $Mn^+(^5S)$ with CS_2 and COS. These results suggest that the $Mn^+(^5S)$ first excited state is approximately 30 times more reactive towards CS_2 than the $Mn^+(^7S)$ ground state.

The cross section for MnS^+ formation in the Mn^+/COS system exhibits two features that are assigned to the spin-forbidden formation of the $MnS^+(^5\Pi)$ ground state and the spin-allowed formation of the $MnS^+(^7\Pi)$ excited state. Similar behavior is expected for the other systems studied in this work, although state-specific features in the product cross sections are not resolved in these systems. However, in all three of these systems, the cross sections have unusual energy dependences that are reproduced much more accurately if two processes are included in the modeling.

The $CrCS^+$, $MnCS^+$, and $CrCO^+$ product cross sections exhibit two endothermic features, which are attributed to the formation of different isomers. At low energies, the $M^+–C–X$ isomers are formed exclusively, while at higher energies the $C–M^+–X$ isomers may be accessed. This assignment is consistent with all experimental evidence, but the possibility that the higher energy features could correspond to excited electronic states of the $M^+–C–X$ isomers or $M^+–X–C$ isomers cannot be definitively eliminated. The results of the Cr^+/CS_2 system suggest that the initial step in the activation of CS_2 by Cr^+ is insertion of the metal into one of the C–S bonds. All of the observed products are consistent with specific fragmentations of the inserted $S–Cr^+–C–S$ species. Other systems studied here have results that are consistent with analogous mechanisms but there is less direct evidence for these pathways in these systems.

Analysis of the reaction thresholds measured in this work yields bond energies for the corresponding metal sulfide and thiocarbonyl cations: $D_0(Cr^+–S) = 2.68 \pm 0.17$, $D_0(Cr^+–CS) = 1.69 \pm 0.06$, $D_0(Mn^+–S) = 2.52 \pm 0.24$, and $D_0(Mn^+–CS) = 0.83 \pm 0.22$ eV. We also speculatively assign the bond energy for the $SCr^+–C$ isomer as 2.9 ± 0.3 eV.

Acknowledgements

This work was supported by the National Science Foundation, grant no. CHE-9877162. The Berlin group (I.K.,D.S.,H.S.) acknowledges support by the Deutsche Forschungsgemeinschaft, the Volkswagen-Stiftung, and the Fonds der Chemischen Industrie.

References

[1] E.I. Stiefel, in Transition Metal Sulfur Chemistry, E.I. Stiefel, K. Matsumoto (Eds.), ACS Symposium Series 653, American Chemical Society, Washington, DC, 1996; pp 2–38, and references therein.
[2] S. Takakuwa, in Organic Sulfur Chemistry, Biochemical Aspects, S. Oae, T. Okyama, (Eds.), CRC Press, Boca Raton, FL, 1992.
[3] S.J. Lippard, J.M. Berg, Principles of Bioinorganic Chemistry, University Science Books, Mill Valley, CO, 1994.
[4] D. Rehder, Angew. Chem., Int. Ed. 30 (1991) 148.
[5] A. Butler, C.J. Carrano, Coord. Chem. Rev. 109 (1991) 61.

[6] C. Rue, P.B. Armentrout, I. Kretzschmar, D. Schröder, J.N. Harvey, H. Schwarz, J. Chem. Phys. 110 (1999) 7858.
[7] I. Kretzschmar, D. Schröder, H. Schwarz, C. Rue, P.B. Armentrout, J. Phys. Chem. A 104 (2000) 5046.
[8] I. Kretzschmar, D. Schröder, H. Schwarz, C. Rue, P.B. Armentrout, J. Phys. Chem. 102 (1998) 10060.
[9] D. Schröder, I. Kretzschmar, H. Schwarz, C. Rue, P.B. Armentrout, Inorg. Chem. 38 (1999) 3474.
[10] I. Kretzschmar, Energetics and Reactivity of the Binary Transition-Metal Sulfides of the 3rd and 4th Row, Shaker Verlag, Aachen, 1999.
[11] K.M. Ervin, P.B. Armentrout, J. Chem. Phys 83 (1985) 166.
[12] R.H. Schultz, P.B. Armentrout, Int. J. Mass Spectrom. Ion Processes 107 (1991) 29.
[13] P.B. Armentrout in Advances in Gas Phase Ion Chemistry, N.G.Adams, L.M. Babcock (Eds)., JAI, Greenwich, CT, 1992, Vol. 1, pp. 83–119.
[14] F.A. Khan, D.L. Steele, P.B. Armentrout, J. Phys. Chem. 99 (1995) 7819.
[15] Y.-M. Chen, P.B. Armentrout, J. Chem. Phys. 103 (1995) 618.
[16] C.L. Haynes, P.B. Armentrout, Organometallics 13 (1994) 3480.
[17] E.R. Fisher, B.L. Kickel, P.B. Armentrout, J. Chem. Phys. 97 (1992) 4859.
[18] P.R. Kemper, M.T. Bowers, J. Phys. Chem. 95 (1991) 5134.
[19] L.S. Sunderlin, P.B. Armentrout, J. Phys. Chem. 92 (1988) 1209.
[20] The ADF package is available from: G. te Velde, E. J. Baerends, Department of Theoretical Chemistry, Vrije University, Amsterdam, The Netherlands, 1995.
[21] E.J. Baerends, D.E. Ellis, Chem. Phys. 2 (1973) 71.
[22] B. te Velde, E.J. Baerends, J. Comp. Phys. (1992) 84, and references cited therein.
[23] J.G. Snijders, E.J. Baerends,. Mol. Phys. 33 (1977) 1651.
[24] S.J,.Vosko, L. Wilk, M. Nusair, Can. J. Phys. 58 (1980) 1200.
[25] M. Levy, J.P. Perdew, Int. J. Quantum Chem. 49 (1994) 539.
[26] J. Sugar, C. Corliss, J. Phys. Chem. Ref. Data 14 (1985) Suppl. 2, 1.
[27] R. Georgiadis, P.B. Armentrout, J. Phys. Chem. 92 (1988) 7067.
[28] L.F. Halle, P.B. Armentrout, J.L. Beauchamp, J. Am. Chem. Soc. 103 (1981) 962.
[29] R.B. Freas, D.P. Ridge, J. Am. Chem. Soc. 102 (1980) 7131.
[30] W.D. Reents, F. Strobel, R.B. Freas, J. Wronka, D.P. Ridge, J. Phys. Chem. 89 (1985) 5666.
[31] E.R. Fisher, P.B. Armentrout, J. Am. Chem. Soc. 114 (1992) 2049.
[32] G. Gioumousis, D.P. Stevenson, J. Chem. Phys. 29 (1958) 294.
[33] M.A. Spackman, J. Phys. Chem. 93 (1989) 7594.
[34] T. Su, M.T. Bowers, in Gas Phase Ion Chemistry, M.T. Bowers (Ed.), Academic, New York, 1973; Vol. 1, p 88. Please note typographical error in Eq. (1)7 of this reference. The denominator of the last term in parentheses should be $\mu^{1/2}\nu$.
[35] M.E. Weber, J.L. Elkind, P.B. Armentrout, J. Chem. Phys. 84 (1986) 1521.
[36] D.A. Prinslow, P.B. Armentrout, J. Chem. Phys. 94 (1991) 3563.
[37] M. Zhou, L. Andrews, J. Phys. Chem. A 104 (2000) 4394.
[38] J.R.Taylor, An Introduction to Error Analysis, University Science Books, Mill Valley, CA, 1982.
[39] K.J. Miller, J. Am. Chem. Soc. 112 (1990) 8533.
[40] W.G. Richards, Trans. Faraday Soc. 63 (1967) 257.
[41] R.K. Nesbet, J. Chem. Phys. 40 (1965) 3619.
[42] I. Butler, Acc. Chem. Res. 10 (1977) 359.
[43] P.B. Armentrout, B.L. Kickel, in Organometallic Ion Chemistry, B.S. Freiser (Ed.), Kluwer Academic, Dordrecht, 1996, p. 28.
[44] D.E. Clemmer, J.L. Elkind, N. Aristov, P.B. Armentrout, J. Chem. Phys. 95 (1991) 3387.
[45] N.Aristov, P.B. Armentrout, J. Am. Chem. Soc. 108 (1986) 1806.
[46] R.L. Hettich, B.S. Freiser, J. Am. Chem. Soc. 106 (1986) 2537.
[47] E.R. Fisher, J.L. Elkind, D.E. Clemmer, R. Georgiadis, S.K. Loh, N. Aristov, L. Sunderlin, P.B. Armentrout, J. Chem. Phys. 93 (1990) 2676.
[48] A. Fiedler, I. Kretzschmar, D. Schröder, H. Schwarz, J. Am. Chem. Soc. 118 (1996) 9941.
[49] F.A. Khan, D.E.Clemmer, R.H. Schultz, P.B. Armentrout, J. Phys. Chem. 97 (1993) 7978.
[50] M.W. Chase, Ed.; J. Phys. Chem. Data, Monograph No. 9; Am. Chem. Soc., 1998.
[51] J.B. Pedley, R.D. Naylor, S.P. Kirby, Chapman and Hall: London, 1986.